

Biomechanics of Joints and Orthopaedic Implants

Professor Sanjay Gupta

Department of Mechanical Engineering

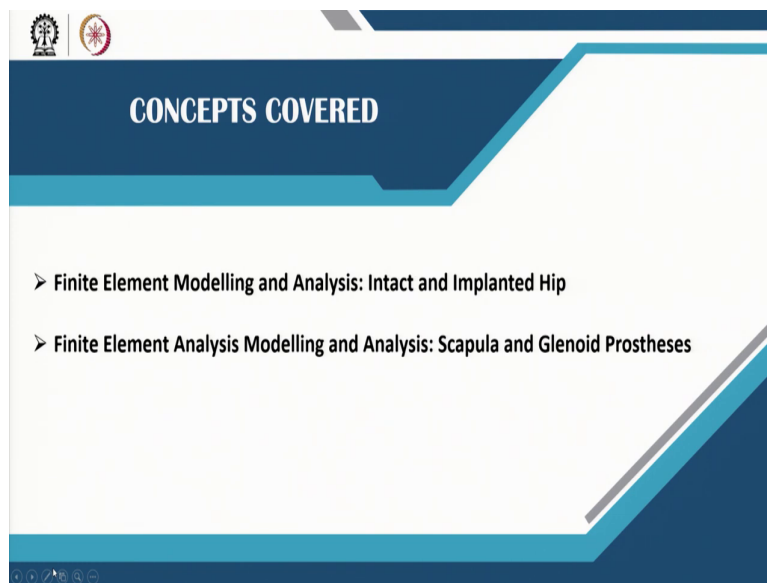
Indian Institute of Technology, Kharagpur

Lecture 31

Finite Element Modelling and Analysis of Hip and Shoulder

Good morning everybody. Welcome to the lecture, lecture 3 in module 6 on Finite Element Modelling and Analysis of Hip and Shoulder.

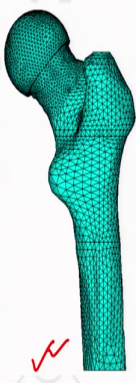
(Refer Slide Time: 00:44)



In this lecture, we will discuss finite element modelling and analysis of intact and implanted hip. So, specifically the femur and the pelvic bone. Later in the lecture, we will discuss finite element analysis and modelling of the scapula and glenoid prostheses.

(Refer Slide Time: 01:08)


Finite Element Analysis: Intact and Implanted Femur



- Contour data from CT slices (layer reconstruction)
- Apparent density vs. CT-grey value (HU) (linear calibration); $\rho = 0.11837 + 0.001141 \text{ HU}$
- Elastic modulus vs. apparent density (power law); $E = 7281 \rho^{1.52}$; E in MPa, ρ in $\text{g}\cdot\text{cm}^{-3}$

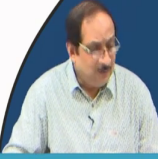
↓

A FE model of bone (97914 elements), where each bone element is assigned individual material properties, based on CT-grey value.



NPTEL Online Certification Courses

IIT Kharagpur

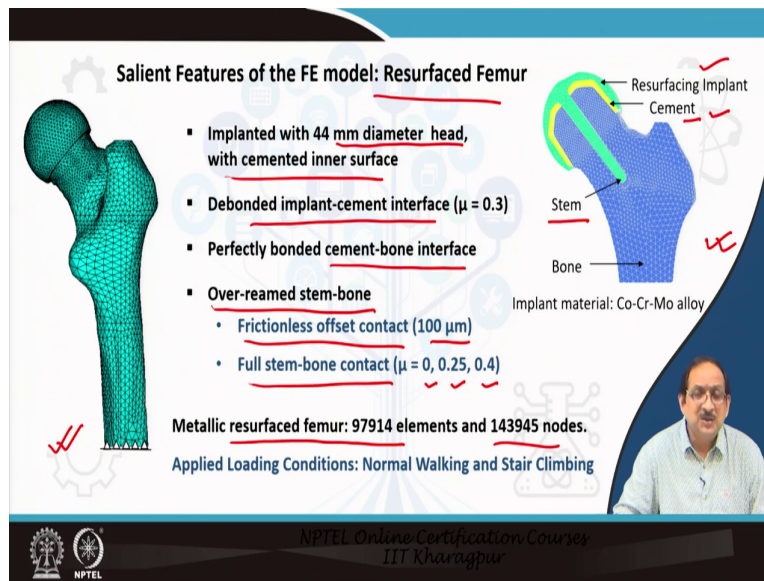


Let us discuss the first topic of this lecture, finite element analysis of intact and implanted femur. Now the finite element model of the intact femur was based on the CT scan data set of a subject. The solid model of the femur bone was based on the contour data from the CT scan slices and using the layer reconstruction method.

Now, from the solid model, we had developed the finite element model, and each element of the finite element model was allocated individual material properties based on linear relationships between apparent density and CT grey value as stated in the slide, and after that, the power-law relationship between the elastic modulus and apparent density as also stated in the slide.

Now, on the left, you can see the finite element model of the intact femur, it contained 97,914 elements, and in this model, each bone element was assigned individual material properties based on CT grey value.

(Refer Slide Time: 03:01)



Now, let us discuss the salient features of the implanted model. In this case, the implanted femur model is a resurfaced femur model as stated in the slide. So, a full model of the resurfaced femur is shown on the left whereas a coronal section of the finite element model has been presented on the right.

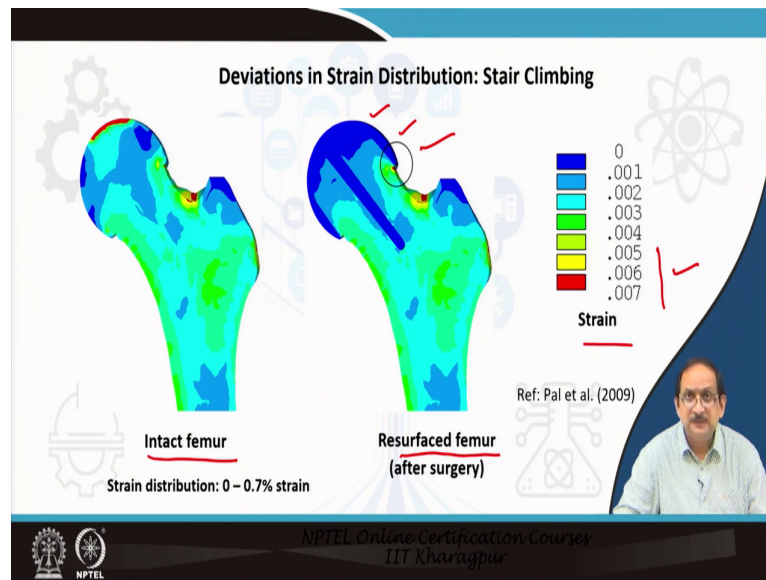
So, the femur was implanted with a 44 mm diameter femoral resurfacing implant and the inner surface of the implant was cemented as indicated here in the figure. So, we have, on the right we have the green coloured resurfacing femoral implant, and the yellow colour is this cemented inner surface.

The implant also had a stem that goes inside an over reamed hole. Now, the implant cement interface was assumed to be debonded with a friction coefficient equal to 0.3. Whereas the cement bond interface was considered to be perfectly bonded. As you can see here, the stem in the figure was inserted into a parallel side hole through the femoral neck and over reamed along its entire length, and this was modelled as completely debonded.

Now, the over ream stem bone condition had different contact conditions simulated in the FE analysis. So, the first contact condition was frictionless offset. We had a gap or offset of 100 microns whereas, for stem bone contact, we assumed different friction coefficients starting from 0.25 and 0.4. So, here also, the metallic resurfaced femur model had 97914 elements and 143945 nodes.

The applied loading conditions used for the simulations were normal walking and stair climbing. So, the musculoskeletal loading condition corresponding to normal walking and stair climbing was used in the FE analysis.

(Refer Slide Time: 06:09)



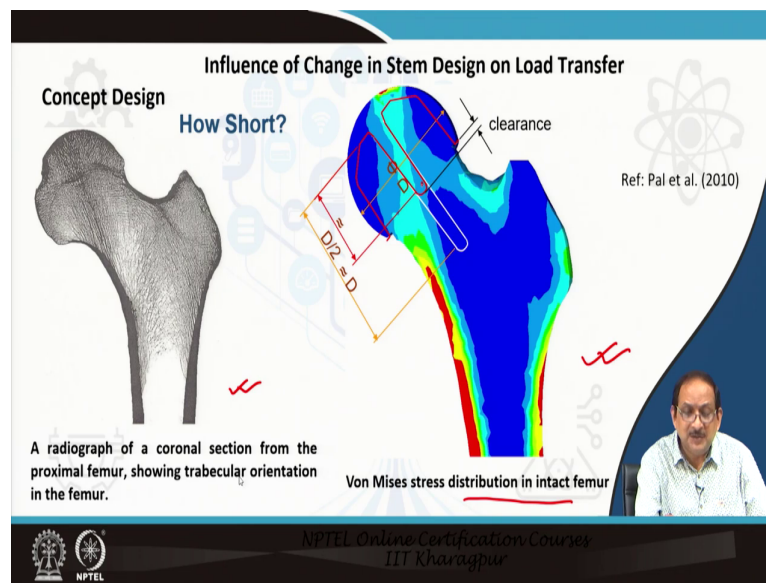
Now, let us present the results. So, in this slide, we have on the left the strain distribution corresponding to the intact femur, and on the right, we have the strain distribution corresponding to the resurfaced femur immediately after surgery. So, the strain contour map is indicated on the right.

So, postoperatively it is observed that there is substantial strain shielding as indicated here in the strain distribution figure. So, the reduction in the strain of 20 to 70 per cent compared to the intact femur was observed inside the proximal femur ahead of the resurfaced femur after surgery.

The resurfacing procedure leads to elevated strain in the range of 0.5 to 0.7 per cent strain around the proximal femoral neck region, particularly around the proximal neck implant junction as indicated by the encircled area in the slide, irrespective of the variation in stem bone contact condition.

This is very close to the yield strain of femoral neck cancellous bone, which is around 0.6 to 0.7 per cent. Clinical studies reported that one of the major concerns of hip resurfacing arthroplasty is the risk of femoral neck fracture during the first few months after surgery.

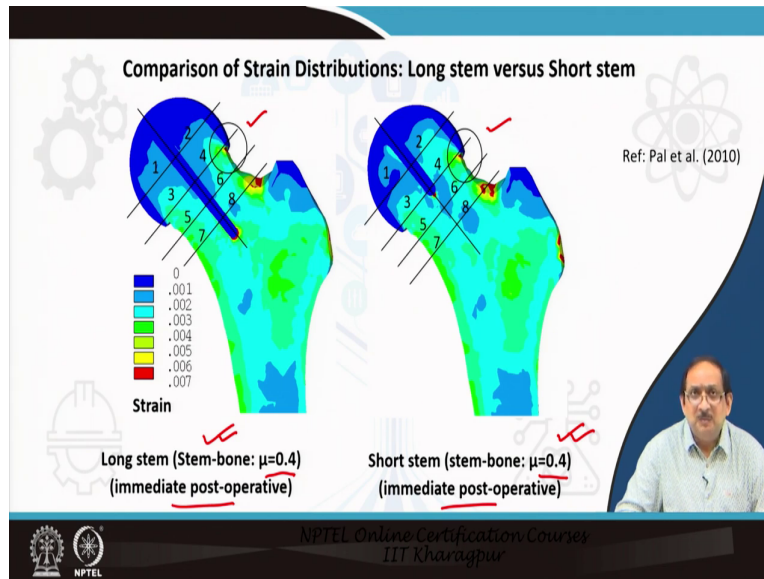
(Refer Slide Time: 08:22)



Now, let us consider the influence of change in stem design on load transfer. So, in this slide on the left, there is a radiograph of a coronal section from the proximal femur, showing trabecular orientation. So, we wanted to change the design of the stem by reducing the stem size, but the question was how much should we shorten the stem size. The objective was to mimic the physiological stress distribution as indicated in the slide.

So, we see that the von Mises equivalent stress distribution in the femur is plotted in the slide and the objective of the change in design is to mimic the stress distribution in the intact femur. So, as you can see, the stem length in the revised design has been reduced to half of the original length and is equal to or approximately equal to the diameter of the resurfacing implant. The other important aspect of this design is to have the stem's tip closer to the centre of the femoral head.

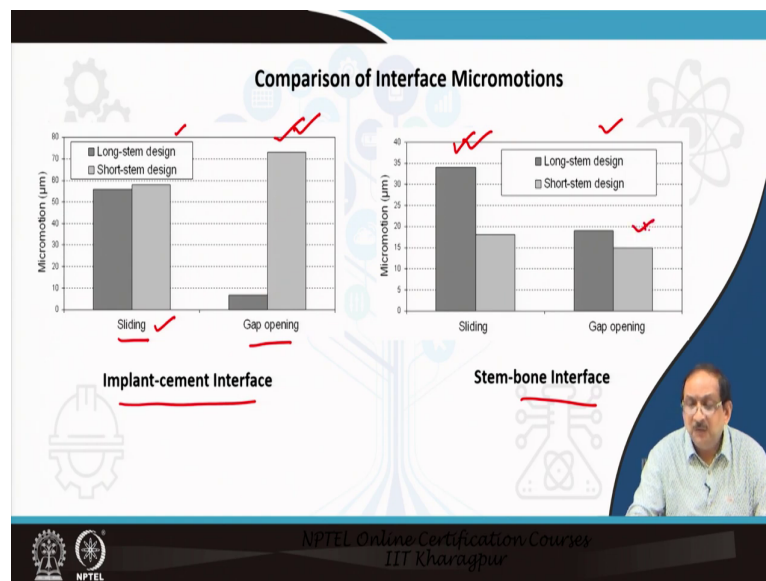
(Refer Slide Time: 10:18)



Let us now compare the strain distributions in the case of the long stem model and the short stem model. On the left, we have presented the strain distribution corresponding to the long stem resurfacing implant. On the right, we have presented the short stem resurfacing implant. These strain distributions correspond to the immediate post-operative situation for both the cases, having the stem bone contact condition μ is equal to 0.04.

It can be observed that the short stem resurfacing implant generates more physiological stress distribution than the long stem. This is very clearly evident in the figure as presented in the slide. It also develops less strained concentration. If we consider the magnitude of the strain at the proximal femoral neck implant junction, the strain concentration, the magnitude of the elevated strain is less in the case of the short stem implant as compared to the long stem implant.

(Refer Slide Time: 12:22)



Now, if we compare the interface micromotions at the implant cement interface and the stem bone interface for the long stem design and the short stem design, we observe certain differences as indicated in the slide. Now, the interface micromotions are of two types; one is the sliding micromotion, the other is gap opening.

Sliding or relative movement at the interface is along the interface, whereas the gap opening is normal. So, if we observe the micro motions in the implant cement interface, we observe that the sliding micromotions are almost similar for the long stem and the short stem design.

However, the gap opening is considerably greater in the case of short stem design as compared to the long stem design as indicated here in the slide. This happens in the case of implant cement interface. Now, if we move to the stem bone interface, we can see that sliding micro motion is less, almost half in the case of short stem design as compared to the long stem design. However, the gap opening for both the designs are almost similar.

(Refer Slide Time: 14:21)

A Summary of Findings: Hip Resurfacing Femoral Implant

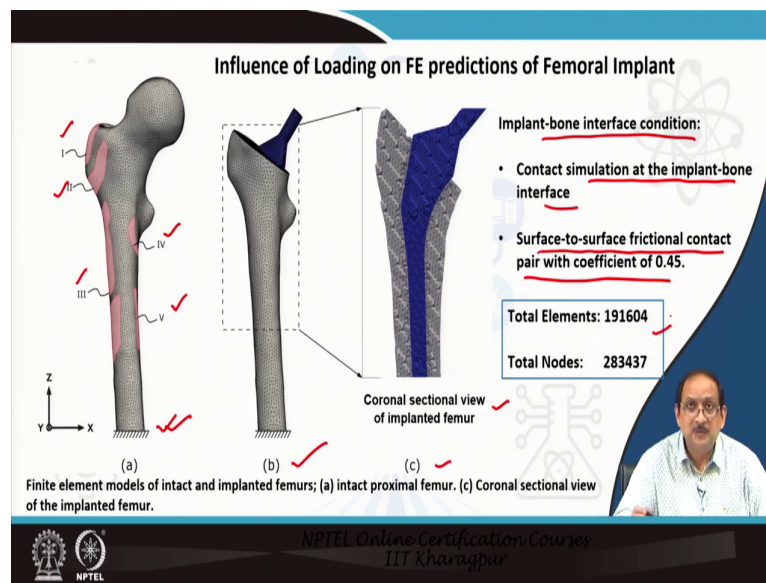
- The contact condition of the metaphyseal stem with surrounding bone has major influence on the stress, strain distribution within the resurfaced femur.
- Strain concentration generated, post-operatively, at the proximal femoral neck region indicated a potential risk of neck fracture.
- The mechanical role of the metaphyseal stem in the resurfaced femur has been observed to be crucial. Shortening the stem length to half the current length led to more physiological stress distribution.
- Reduced effect of strain shielding, reduction of strain concentration in cancellous bone around the proximal femoral neck region and the distal tip of the stem.

NPTEL Online Certification Course
IIT Kharagpur

Let us come to the summary of findings. In case of this hip resurfacing femoral implant. The contact condition of the metaphyseal stem with surrounding bone has major influence on the stress-strain distribution within the resurfaced femur. The strain concentration generated postoperatively at the proximal femoral neck region indicated a potential neck fracture risk within a few months after surgery.

The mechanical role of the metaphyseal stem in the resurfaced femur has been observed to be crucial; shortening the stem length to half the current length lead to a more physiological stress distribution. Reduced effect of strain shielding, reduction of strain concentration in the cancellous bone around the proximal femoral neck region and at the distal tip of the stem was observed in case of short stem implant.

(Refer Slide Time: 15:38)



Now, let us consider another study wherein we will be discussing a conventional total hip replacement and as you can see from the figure that a femoral implant has been virtually implanted and an uncemented femoral implant has been virtually implanted inside the bone, on the same bone on which the FE model of the natural femur has been developed.

So, on the left, we have the intact or natural femur model with the muscle attachment sides, so there are five muscles here like gluteus minimis, vastus lateralis, vastus medialis, vastus, vastus intermedius and abductor muscles as indicated in the figure 1, 2, 3, 4 and 5. Now, the figure B presents the implanted femur and the figure c presents the coronal section of the implanted femur with the implant clearly visible inside the bone.

The implant-bone interface conditions is presented here in the slide. So, contact simulation at the implant-bone interface was employed using the surface-to-surface frictional contact elements with the coefficient of friction of 0.45. So, the total number of elements was around 200,000.

(Refer Slide Time: 17:41)

3D FE Modelling of Intact and Implanted Femur

- An image processing software, MIMICS (Materialise, Leuven, Belgium) was used for generating 3D surface geometry of the right intact femur. A 3D model of the TriLock uncemented hip stem (DePuy Orthopaedics, Warsaw, IN) was used in the analysis.

- 10-node tetrahedral elements ✓
- Each bone element is linear, elastic and isotropic ✓
- Surface-to-surface frictional contact pair with coefficient of 0.45 ✓

$$\rho = \rho_1 + (\rho_2 - \rho_1) \times \frac{HU - HU_1}{HU_2 - HU_1}$$

$(\rho_1, HU_1) : 0.022 \text{ gm.cm}^{-3}, 0 \text{ HU}$
 $(\rho_2, HU_2) : 1.73 \text{ gm.cm}^{-3}, 1700 \text{ HU}$

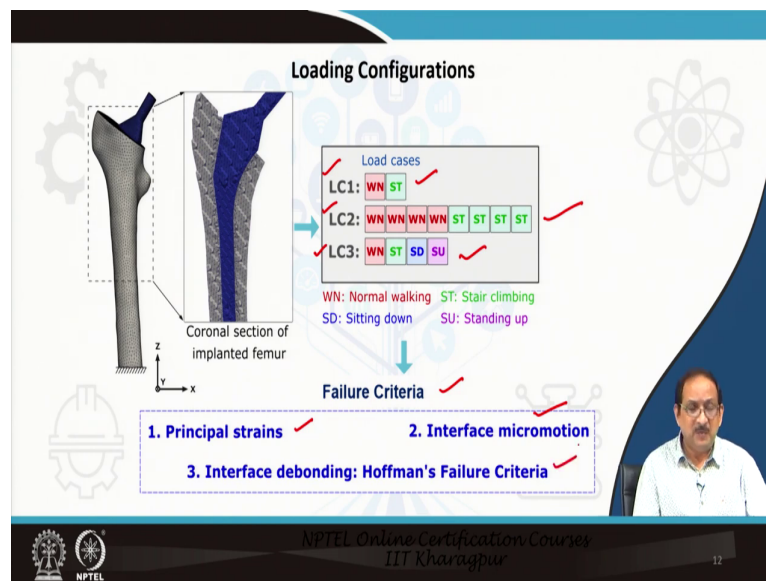
Young's Modulus of bone element assigned based on: $E = 7281 \rho^{1.52}$ (in MPa) ✓
Young's Modulus of the implant material: 110 GPa (Titanium Alloy)

NPTEL Online Certification Courses
IIT Kharagpur

Now, the 3D FE modelling of the intact and implanted femur was based on CT scan data. So, an image processing technique using mimics was used to generate 3D surface geometry of the right intact femur. A 3D model of the trial of the uncemented hip stem was used in the analysis. So, the model meshed with 10-node tetrahedral elements; each element is considered to be linear or assumed to be linear, elastic and isotropic.

There is surface to surface frictional contact elements with a coefficient of friction 0.45 in the contact simulation employed at the implant-bone interface. As discussed earlier, the apparent density of a bone element can be calculated based on the patient's specific CT scan data set and the Young's modulus of the bone element can be assigned using the power-law relationship between Young's modulus and apparent density. The Young's modulus of implant material is titanium alloy. So, Young's modulus value is 110 GPa.

(Refer Slide Time: 19:14)

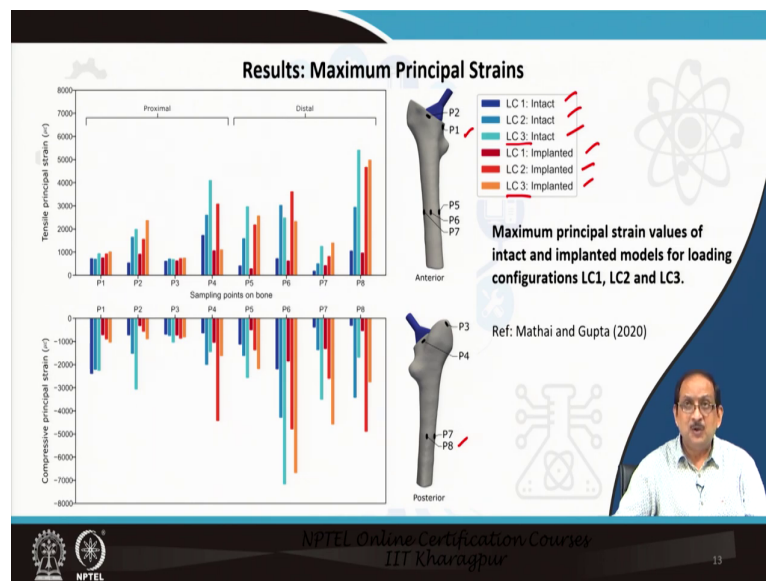


The loading configurations used in this analysis actually vary, there are three loading configurations LC 1, LC 2 and LC 3 and we are now going to investigate the effect of different loading configurations on the failure criteria and the stress-strain distribution. So, loading configuration 1, consists of two load cases. It is the maximum load cases during heel contact of normal walking and stair climbing.

So, we have two load cases, the maximum load cases during heel contact of normal walking and stair climbing, the loading configuration 2 consist of 8 load cases out of which 4 load cases are for the normal walking cycle and 4 load cases are for the stair climbing cycle.

LC 3 or the loading configuration 3 included the maximum load cases from other everyday activities like sitting up from the chair and sitting down on the chair along with the peak load cases of normal walking and stair climbing, peak load instances of hip contact forces were considered for these activities. Now, we will be investigating the failure criteria and we will be looking into principals strains interface micromotion and interface debonding using Hoffman's failure criteria.

(Refer Slide Time: 21:16)

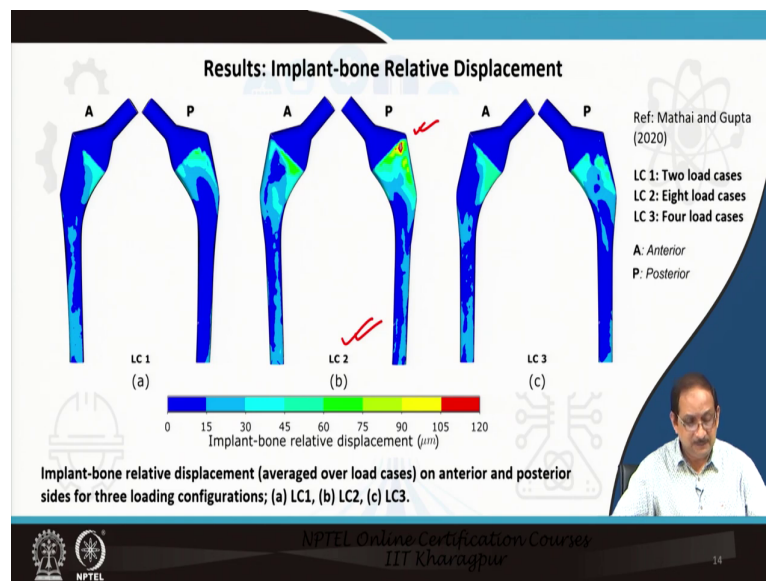


So, let us look into the results of the maximum principal strains. So, here in this figure, principal strains, tensile and compressive were estimated at eight locations. So, P 1 to P 8 at 8 locations on the proximal and distal regions of the intact and implanted FE models. So, the blues set corresponds to the intact model results and red and orange, reddish and orange correspond to the implanted model results.

Now among the three loading configurations, the LC 3, the loading condition configuration 3 predicted the highest tensile and compressive strain values in the majority of the locations. In the implanted female LC 3, repeat LC 3 predicted maximum tensile and compressive strain in most locations except 0.3 0.4 0.6 and 0.8 similar to the intact models.

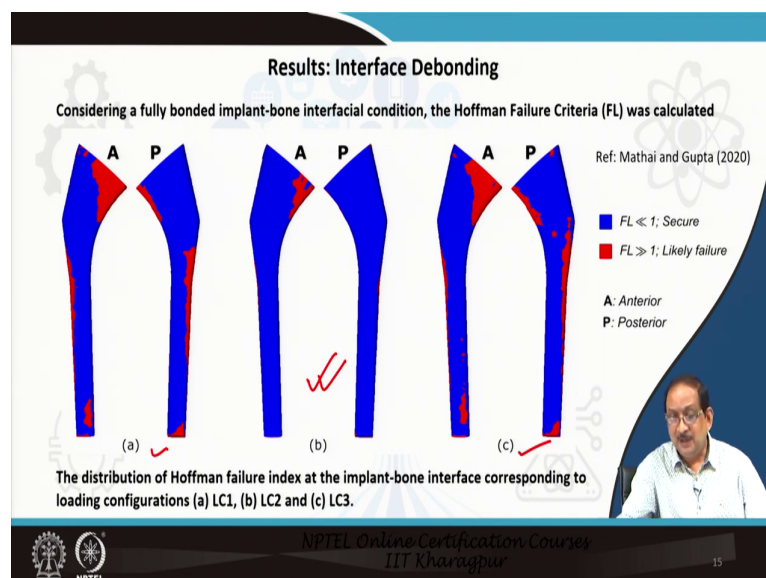
However, at 0.4 and 0.8 LC 2 reported the highest principal strains of 3200 microstrain and 4000 microstrain respectively at the posterior region P 5 to P 8 0.5 to 0.8. The implanted model experienced 50 percent to 75 percent increase in principal strains, then those of the intact models.

(Refer Slide Time: 23:24)



Now, let us look into more results on implant-bone relative displacement. Now, in this figure, we are presenting the distribution of average implant-bone relative displacement. The proximal part or the Caulker of the implant experienced high repeat, relatively high micro motions, repeat relatively high implant-bone relative displacement in the order of 40 micron to 120 micron as compared to other regions for all loading configurations. However, the loading configuration 2, a relative displacement of 110 micron was observed at the posterior part of the implant.

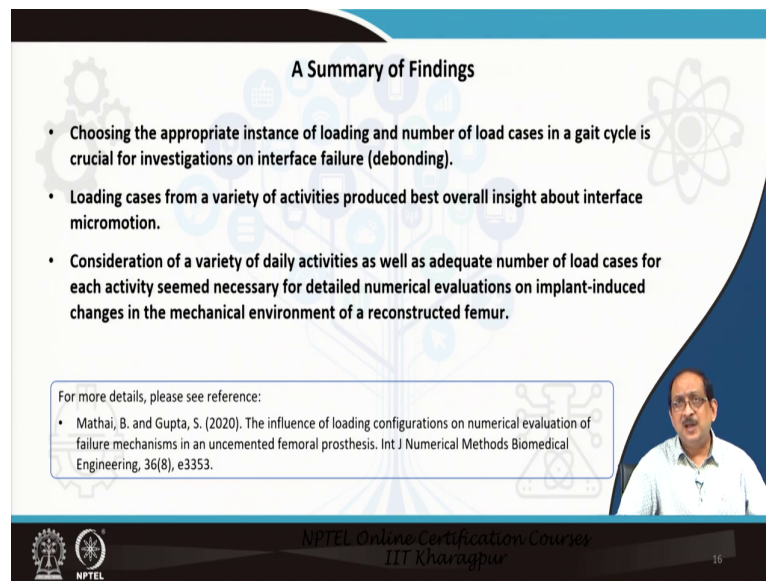
(Refer Slide Time: 24:43)



Let us now consider the distribution of Hoffman failure criteria at the implant-bone interface for different loading configurations as presented in the figure. A similar pattern of the Hoffmann failure criteria was observed at the anterior medial part of implant for the load cases 1 and 3.

In comparison, the load case 2 predicted least susceptible area of failure. So, area of failure is actually indicated in the graph as FL greater than 1. So, the LC 2 predicted the least susceptible area of failure among all loading configurations as indicated clearly in the figure.

(Refer Slide Time: 25:54)



A Summary of Findings

- Choosing the appropriate instance of loading and number of load cases in a gait cycle is crucial for investigations on interface failure (debonding).
- Loading cases from a variety of activities produced best overall insight about interface micromotion.
- Consideration of a variety of daily activities as well as adequate number of load cases for each activity seemed necessary for detailed numerical evaluations on implant-induced changes in the mechanical environment of a reconstructed femur.

For more details, please see reference:

- Mathai, B. and Gupta, S. (2020). The influence of loading configurations on numerical evaluation of failure mechanisms in an uncemented femoral prosthesis. *Int J Numerical Methods Biomedical Engineering*, 36(8), e3353.

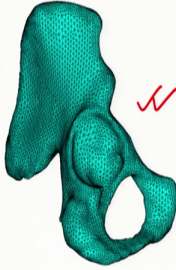
NPTEL Online Certification Courses
IIT Kharagpur

Now, let us come to the summary of findings for this study. Choosing the appropriate instance of loading and the number of load cases in a gate cycle is crucial for investigation on interface failure or debonding, loading cases from a variety of activities produced best overall insight about interface micromotion.

Consideration of a variety of daily activities as well as the adequate number of load cases for each activity seem necessary for detailed numerical evaluations on implant induced changes in the mechanical environment of a reconstructed femur.

(Refer Slide Time: 26:39)


Finite Element Modelling and Analysis: Pelvic Bone




- Image processing of CT- scan data slices ✓
- Apparent density vs. CT- grey value (linear calibration): $\rho = 0.022 + 0.001038 \text{ HU}$ ✓
- Elastic modulus vs. apparent density of cancellous bone (power law): $E = 2017.3 \rho^{2.46}$ ✓
- Cortical bone $E = 17 \text{ GPa}$

↓

A FE model of the pelvic bone containing 221947 number of elements was developed based on a subject-specific CT-scan dataset, where each bone element was assigned individual material properties, based on CT-grey value.

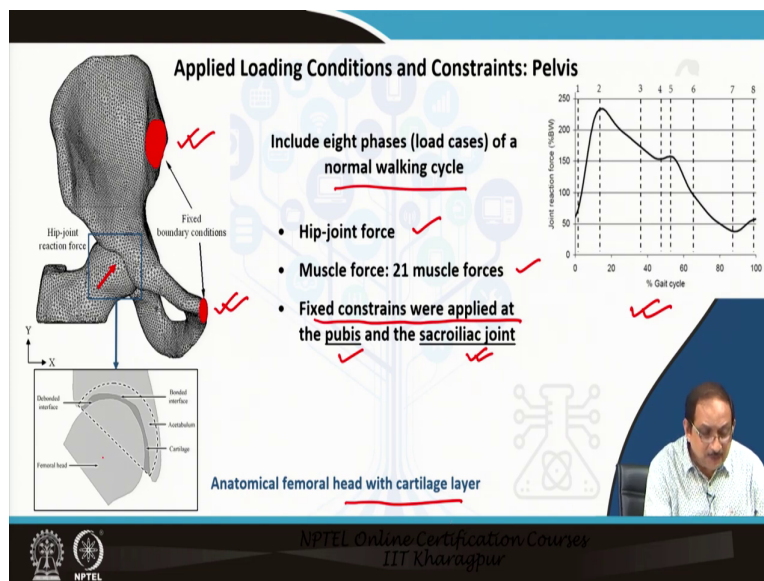


NPTEL Online Certification Courses
IIT Kharagpur

Let us now focus on the finite element modelling and analysis of a pelvic bone, here I reintroduced the slide that was discussed earlier in lecture 6.2, the procedure of development of a finite element model of the pelvic bone based on CT scan data. So, we can obtain a solid model from image processing of CT scan data slices and then generate the mesh to develop a finite element model.

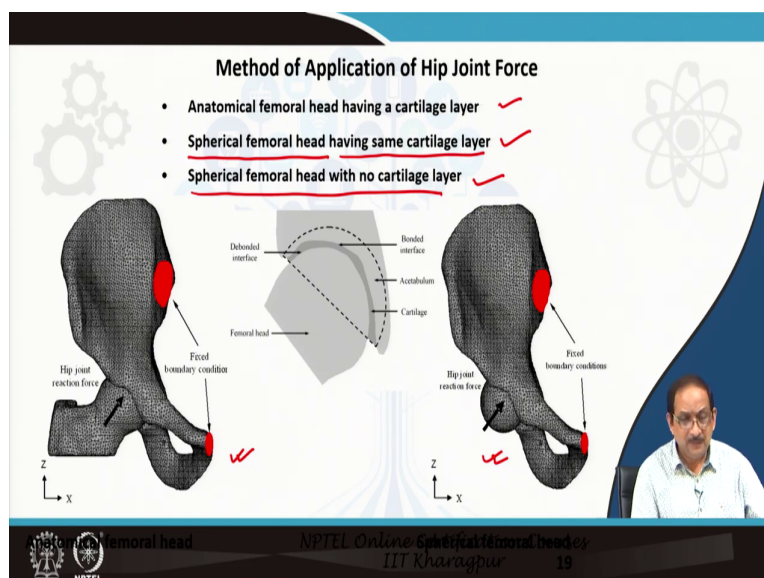
The material properties of the bone elements can be assigned based on the CT grey value and we have already discussed these aspects quite elaborately, using the linear calibration and the power-law relationship, we can actually assign Young's modulus to each and every bone element of the finite element model of the pelvic bone. So, here you can see that the pelvic bone model contains 221947 elements.

(Refer Slide Time: 28:01)



Now, the applied loading conditions and constraints in the pelvic bone model includes eight, repeat includes eight phases that is load cases, eight load cases of a normal walking cycle as indicated in the figure, these load cases consist of data on hip joint force, 21 muscle forces corresponding to each load case and fixed constraints where applied at the pubis and the sacroiliac joint, similar to the natural hemipelvis and anatomical femoral head with a cartilage layer was also included in the model in order to apply the hip joint reaction force from the centre of the femoral head on to the acetabular cavity.

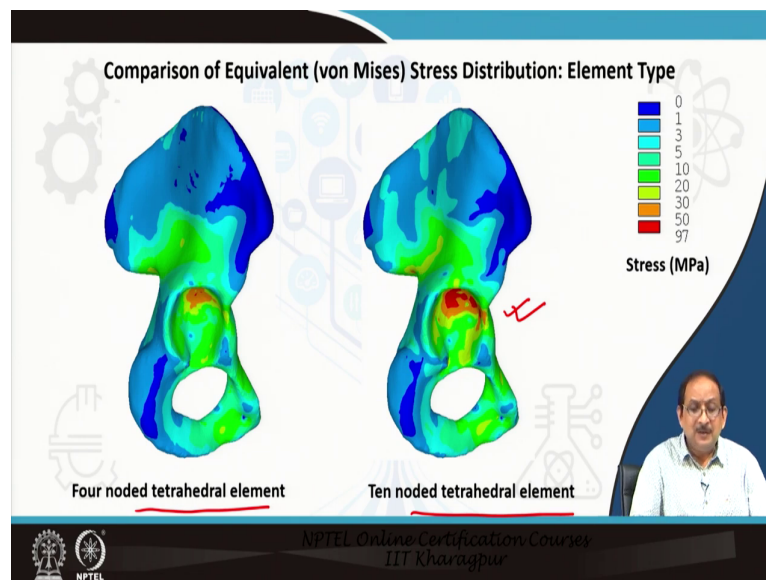
(Refer Slide Time: 29:22)



Now, we investigated the effect of different methods of application of hip joint force. So, we had actually three different models, one with the anatomical femoral head having a cartilage layer. The other model assumed that the femoral head is almost spherical, but not exactly spherical, but we assumed a spherical femoral head for simplicity.

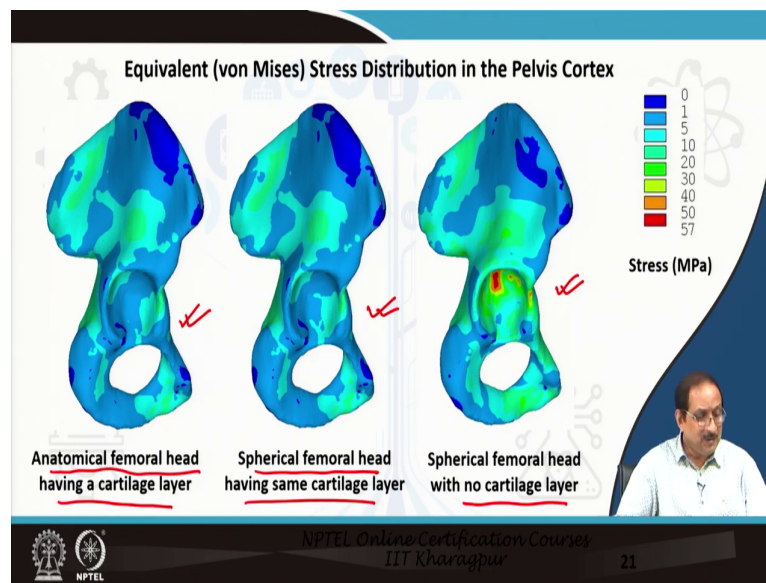
So, this spherical head having the same cartilage layer was used for a second model and the third model had a spherical femoral head with no cartilage as indicated in these two figures, the figure on the left is the first model anatomical femoral head having cartilage layer. Whereas the figure on the right, presents the spherical femoral head, the spherical assumption of the femoral head with and without the cartilage layer.

(Refer Slide Time: 30:42)



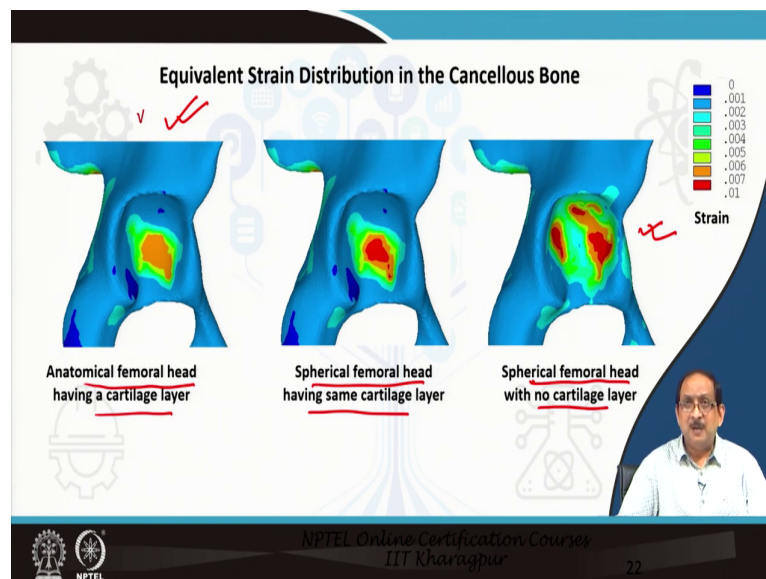
We also investigated the effect of the element type. So, we compared the results corresponding to four noded tetrahedral elements: the tetrahedral element without the mid side node and the 10 noded tetrahedral elements which have the mid-side nodes. So, in this slide, we compare the equivalent stress distribution corresponding to the two different element types. Here you can see that the stresses generated in the 10 noded tetrahedral element model is higher than the 4 noded tetrahedral element model.

(Refer Slide Time: 31:36)



Let's now compare the stress distribution in the pelvic cortex corresponding to different methods of application of the hip joint force as indicated earlier. We see that the anatomical femoral head with the cartilage layer is quite similar to the spherical femoral head having the same cartilage layer. The spherical femoral head without any cartilage layer gives rise to some stress concentration as indicated in the slide within the acetabular cavity.

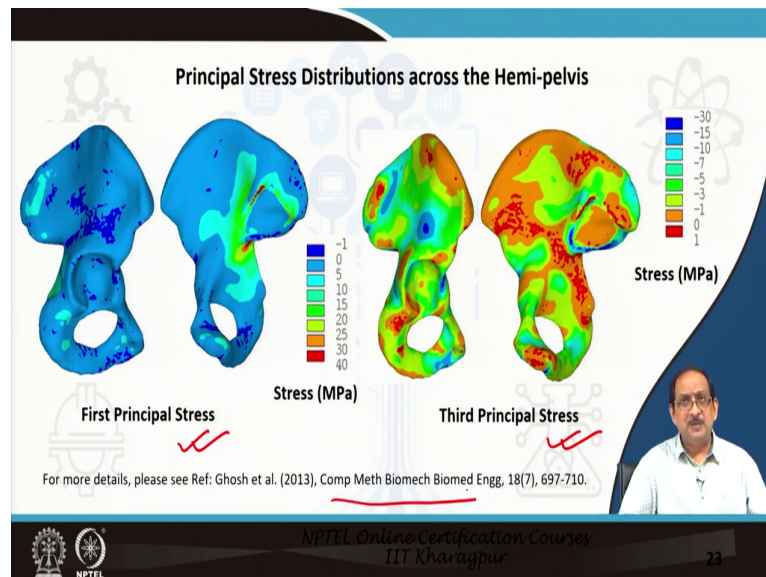
(Refer Slide Time: 32:34)



Now, if we compare the equivalent strain distribution in the cancellous bone, we also see that the strains corresponding to the spherical femoral head without the cartilage layer are higher than the anatomical femoral head with spherical femoral head with the same cartilage layer.

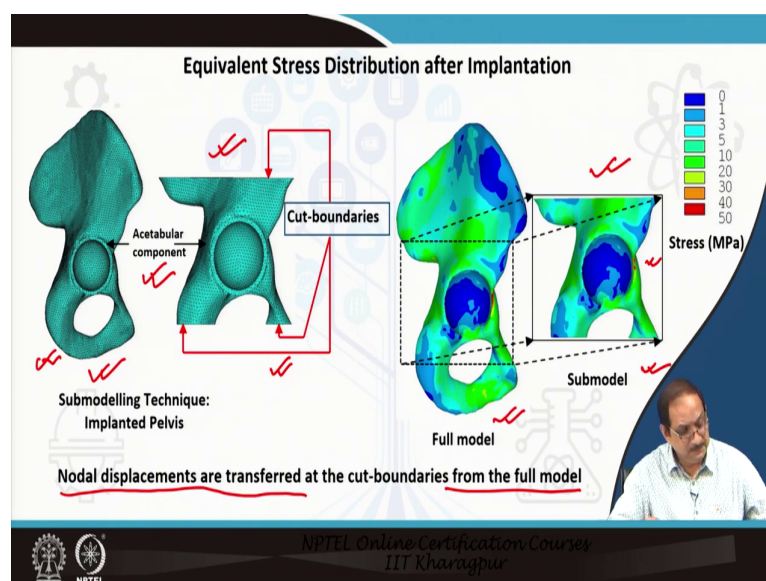
So, we may conclude that the anatomical femoral head having a cartilage layer is the most appropriate method of applying hip joint reaction force or hip joint contact force on the acetabular cavity.

(Refer Slide Time: 33:32)



Now, let us now, let me present the principal stress distribution across the hemipelvis. As you can see in the figure, the first principal stress is plotted on the left in two views, whereas the third principal stress is plotted on the right in two views. For more details about about this study, you may please refer to our published paper in the journal computer methods in biomechanics and biomedical engineering.

(Refer Slide Time: 34:14)



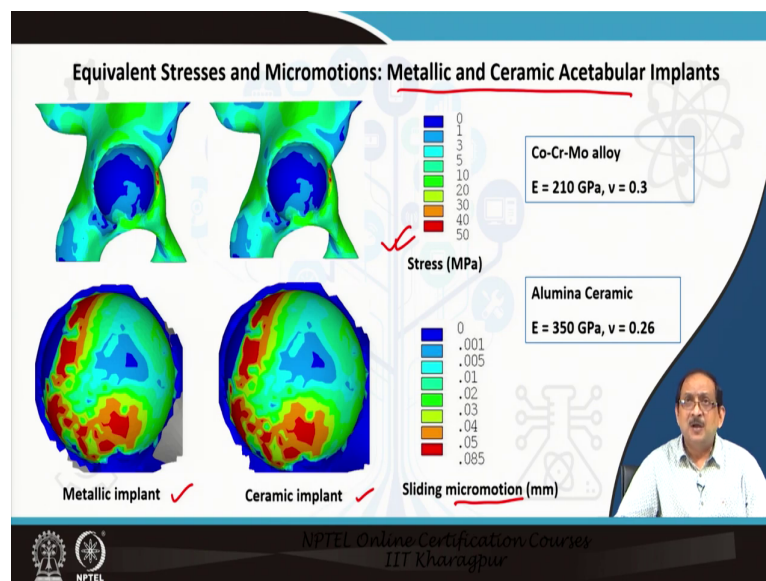
Let us now move into the implanted pelvic bone. As you can see in the figure, we present the implanted pelvis's finite element model with the acetabular component. So, this is a full model of the pelvic bone with the acetabular component. On the right, we have a sub-model of the implanted pelvis with well-defined cut boundaries.

Now, we will be employing this sub modelling technique to focus our investigation in and around the domain of inclusion of the prostheses, the objective of developing a sub model in an implanted as acetabular with a finer mesh around the prostheses is to focus our investigation in the domain of inclusion of the prostheses.

So, at this count cut boundaries, the nodal displacements are transferred from the full model that is, from the full model of the implanted pelvis to the sub model of the implanted pelvis, now the efficacy of this method can be compared as we had done by comparing the stress distribution in both the models.

It is very clear from the results that the stress distribution in both models is very similar. However, only at few locations can the fine difference in stress distribution be observed because this sub model is based on a finer meshed model compared to the full-scale model. So, since this model has a finer mesh, it better describes the variation in bone material properties incorporated within the model.

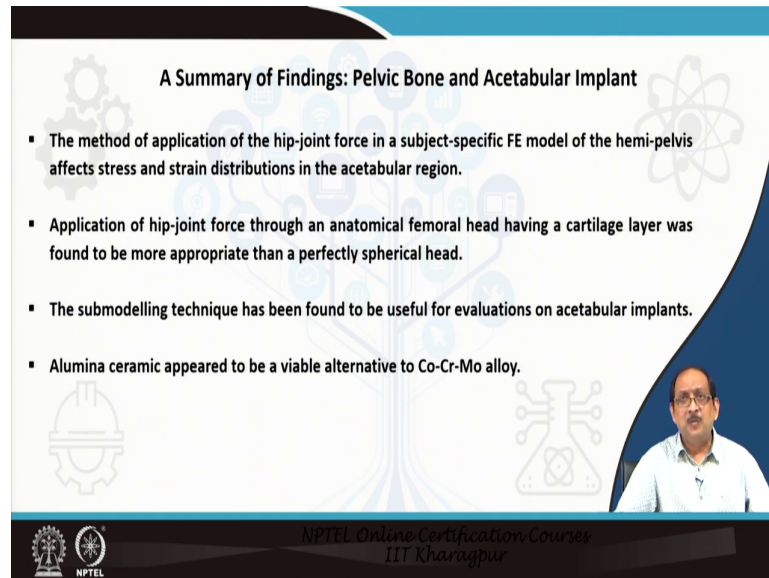
(Refer Slide Time: 36:53)



Let us discuss the given stresses and micromotion in case of metallic and ceramic acetabular implants. So, the figure presented here presents the stresses in the underlying cancellous bone

for the metallic and ceramic implants as well as the micro motions in cases of the metallic and ceramic implants. So, it can be observed that the stresses, as well as the sliding micro motions for both the metallic and the ceramic implants, are quite similar.

(Refer Slide Time: 37:43)



A Summary of Findings: Pelvic Bone and Acetabular Implant

- The method of application of the hip-joint force in a subject-specific FE model of the hemi-pelvis affects stress and strain distributions in the acetabular region.
- Application of hip-joint force through an anatomical femoral head having a cartilage layer was found to be more appropriate than a perfectly spherical head.
- The submodelling technique has been found to be useful for evaluations on acetabular implants.
- Alumina ceramic appeared to be a viable alternative to Co-Cr-Mo alloy.

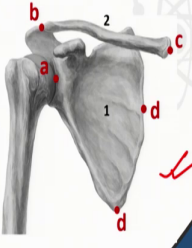
NPTEL Online Certification Courses
IIT Kharagpur

Let me present a summary of the findings of pelvic bone and acetabular implant. The hip joint force application method in a subject-specific FE model of the hemipelvis affects stress-strain distribution in the acetabular region, application of hip joint force through the anatomical femoral head, having a cartilage layer was found to be more appropriate than a perfectly spherical head. The sub-modelling technique has been useful in evaluating acetabular implants and alumina ceramic appears to be a viable alternative to cobalt chrome molybdenum alloy.

(Refer Slide Time: 38:27)

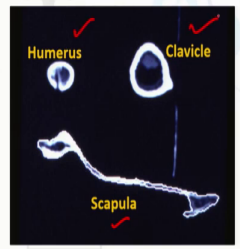
Finite Element Modelling and Analysis: Scapula and Glenoid Prostheses

The shoulder girdle consists of: (1) Scapula, (2) Clavicle, and functions as a movable but stable base for the motions of the humerus.



The shoulder joint comprises of:

- a. GlenoHumeral (GH) joint ✓
- b. AcromioClavicular (AC) joint ✓
- c. SternoClavicular (SC) joint ✓
- d. ScapuloThoracic Gliding Plane (STGP) ✓



CT-scan slice of shoulder ✓

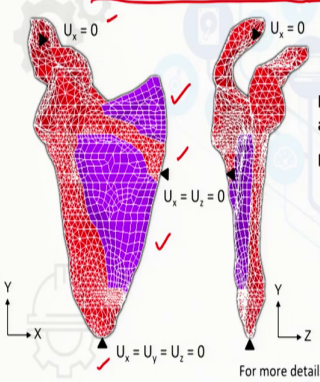
NPTEL Online Certification Courses
IIT Kharagpur

Let us now come to the second part of the lecture on finite element modelling and analysis of the scapula and the glenoid prostheses. So, as discussed earlier, the shoulder girdle consists of the scapula and the clavicle and functions as a moveable but stable base for the motions of the humerus. shoulder joint comprises of the glenohumeral joint, acromial clavicular joint, sternoclavicular joint and scapula thoracic gliding plane as indicated in the figure. A typical CT scan slice of the shoulder is presented here on the left and you can see a section of through the shoulder joint presenting the scapula, humerus and clavicle.

(Refer Slide Time: 39:27)

Finite Element Modelling and Analysis of the Scapula

A combination of shell and solid elements, was used to develop a realistic 3-D (FE) model of the human scapula



Shell elements: outer cortical layer, infraspinous and supraspinous fossa
Solid elements: remaining part of compact bone and trabecular bone

Musculoskeletal model of forces of 17 muscles during 0 – 180° abduction were used as applied loading (Van der Helm, 1994).
Muscle forces were applied on the respective attachment areas.

Elements: 10921 ✓
Nodes: 14086
DOF: 63435

For more details, please see Ref: Gupta and Van der Helm (2004)

NPTEL Online Certification Courses
IIT Kharagpur

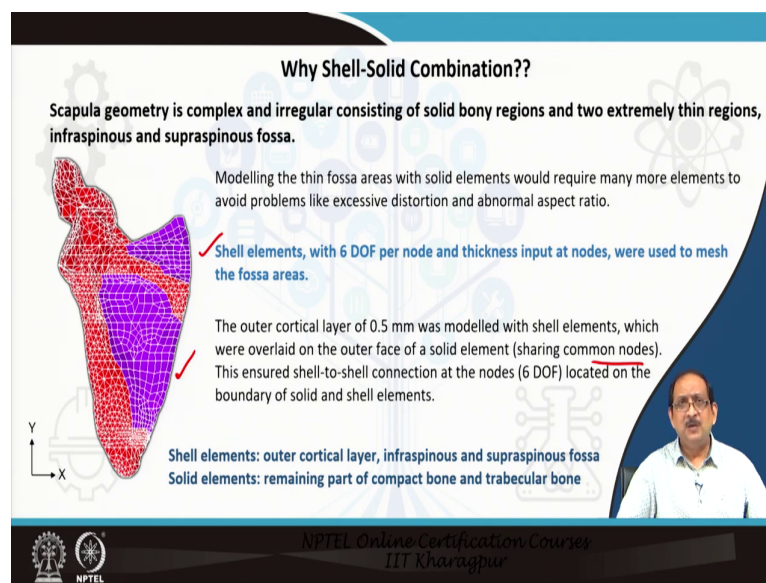
Now we have developed this finite element model of the scapula based on the CT scan data of a scapula. Now, this scapula represents a sandwich structure, since it has an inner core of

cancellous bone covered by an outer layer of cortical bone. Now considering the complexity of the structure of the scapula, a combination of shell and solid elements was used to develop a realistic model of the scapula.

The shell elements represented the outer cortical layer and the fossa area, both the infraspinatus and supraspinous fossa. As indicated in the violet colour, the solid elements were used to represent a part of the compact bone and the cancellous or the trabecular bone.

So, the musculoskeletal skeletal model of forces of 17 muscles during abduction, humeral abduction 0 to 180 degree was used as applied loading conditions and the muscle forces were applied on the respective attachment areas. The model was constrained at three locations, to fix it in space and to avoid rigid body motion. So, the total number of elements generated were about 11,000 elements.

(Refer Slide Time: 41:27)



Now, the question is that why we are choosing a solid shell combination. Now scapula geometry is complex and irregular consisting of solid bony regions and two extremely thin regions infraspinous and supraspinous fossa. Now modelling the thin fossa areas with solid elements would require many more elements to avoid the problems like excessive distortion and abnormal aspect ratio.

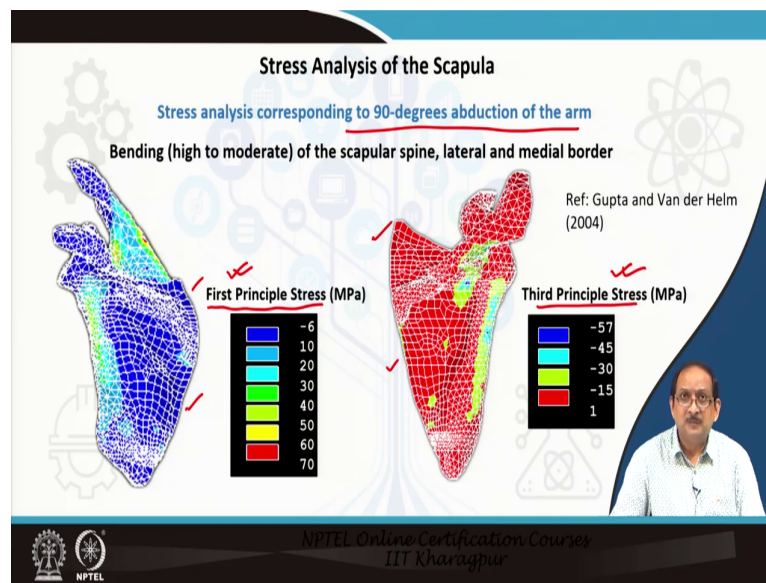
Aspect ratio is defined as the ratio of maximum and minimum dimensions of an element. The shell elements with 6 degrees of freedom per node, 3 rotation and 3 translation and thickness input to add each node were used to mesh the foresight area. The outer cortical layer of 0.5

millimeter was modelled with shell elements and these were overlaid on the outer face of a solid element, sharing common nodes.

This ensured shell to shell connection at these common nodes having 6 degrees of freedom located on the boundary of shell and solid elements, this ensured shell to shell connection at the nodes with 6 degrees of freedom located on the boundary of solid and shell elements. So, the shell is representing.

So, repeat. So, the shell elements represent the outer cortical layer and the fossa area, whereas the solid elements are used to represent the compact bone and the cancellous bone regions.

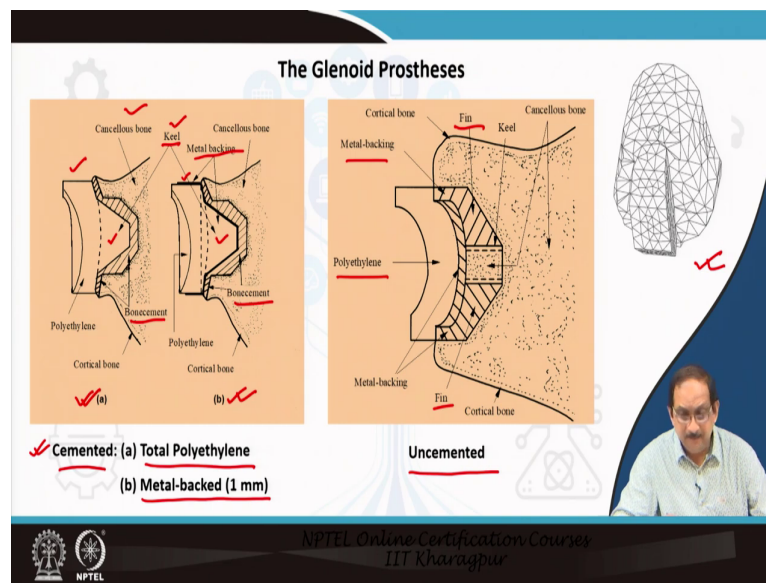
(Refer Slide Time: 43:34)



Let me present to you the stress analysis of the natural scapular corresponding to 90-degree abduction of the arm. Now, here we present two figures. The first principal stress distribution on the left and the third principal stress distribution on the right. So, that we can evaluate the stresses in different parts of the scapula, we observed high tensile and compressive stresses generated on either sides of the scapular spine, lateral border, medial border and acromial which indicates bending of these structures.

Now, stresses were found to be low in the fossa areas, the infraspinatus fossa and the supraspinous fossa in both the views, which indicate that the function of these areas is to act as attachment sites of large muscles the FE model along with this static shoulder model of forces is useful for calculating stress distribution in various parts of the scapula during movements of the arm.

(Refer Slide Time: 45:11)



Let us now discuss about glenoid prostheses. Now, in this slide, we have presented two types of glenoid prostheses, one is the cemented glenoid prostheses, it has actually total, it can be a total polyethylene prosthesis which is indicated by figure a and there may be a metal-backed polyethylene design which is indicated in figure b.

On the right, we have an uncemented design of the glenoid prostheses. Now, let us go one by one. So, we have in this slide presented a sketch of the coronal section within the glenoid. Here in figure a of the cemented variety, we can see that the total polyethylene prostheses and the hatched area is the cemented area.

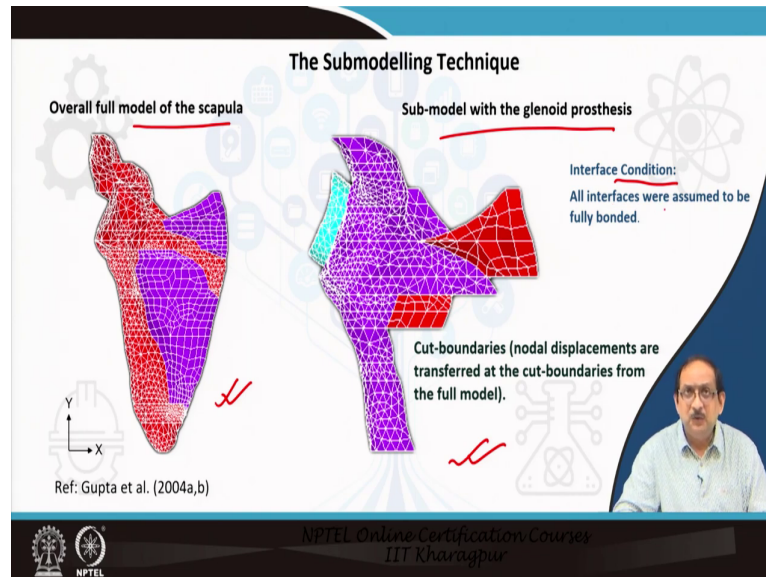
So, that is bone cement and the rest is cancellous bone as indicated in the slide. Now, this total polyethylene prostheses resembles or near prostheses. So, we have a keel in both the designs, the difference between the design of the metal backing is that it has a 1-millimetre metallic shell covering the total polyethylene component.

So, that means it adds a little more rigidity in the implant as compared to the total purely total polyethylene glenoid processes. So, the metal backing is shown here with the thicker black line, the bone cement as usual is used to fix the glenoid prostheses within the glenoid cavity. Now, let us see the uncemented design.

So, in the unsegmented design, we have a far more solid metal backing as indicated by the hatched area. There is a polyethylene on top of the metal backing, but the metal backing consists of two fins along the superior inferior region and there is a hollow cylinder within

which bone can actually grow at the interface. Finite element representation of the cemented glenoid processes is represented on the right-hand corner of the slide.

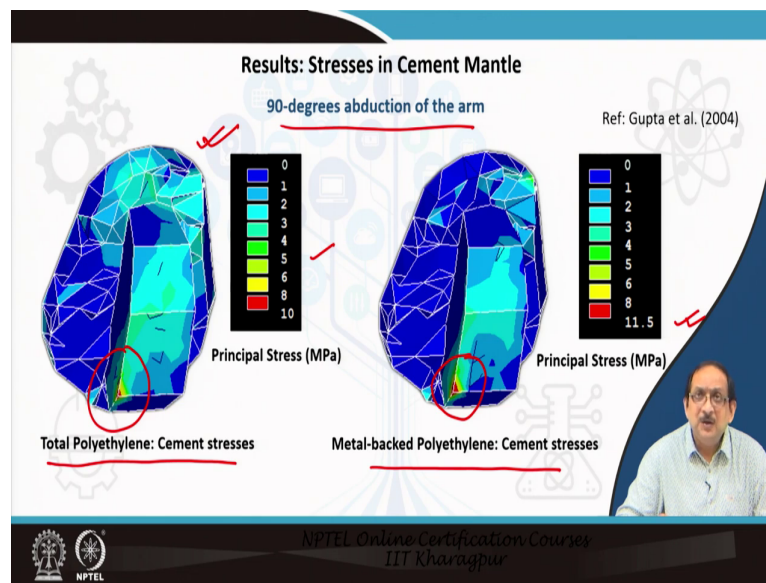
(Refer Slide Time: 48:51)



Now, similar to the pelvic bone, we have also employed the sub modelling technique and this sub modelling technique was used for the numerical investigations on glenoid processes. The objective wants to generate a fine mesh around the prostheses and to focus our investigation in the domain of inclusion of the prostheses.

Now, on the left, we can see the overall full model of the scapula and on the right, we see the sub model of the glenoid prostheses. Now, a link between the full overall model of the scapula and the sub model was established at the cut boundaries by transferring the displacements, the nodal displacements at the cut boundaries from the overall full model of the scapula. The interface condition assumed for this analysis was all interfaces were assumed to be fully bonded.

(Refer Slide Time: 50:13)

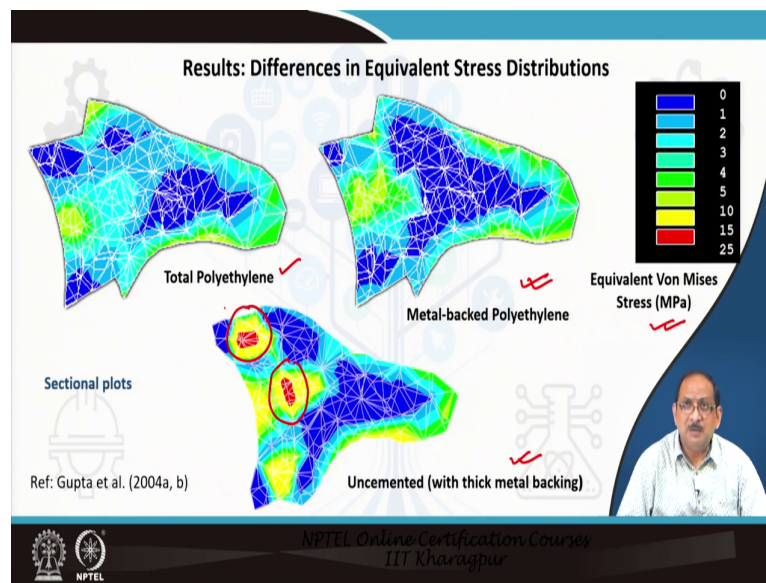


Now, let us move into the results, we first present to you the stresses in the cement mantle. So, the results correspond to 90 degree abduction of the arm, where the glenohumeral joint reaction force was found to be maximum. Now, on the left, we have, we present the cement stresses corresponding to the total polyethylene design and on the right, we present the cement stresses corresponding to the metal-backed design.

Now, in case of total polyethylene design, the tensile stresses generated in the cement generally varied between 0.1 to 5 MPa as you can see in the figure, in the stress distribution, principals stress distribution. However, around the tip of the keel, as you can see here, the stresses in the cement were comparatively higher in the range of 6 to 10 MPa.

In case of metal backed design, almost similar stress distribution within the cement was observed. However, the maximum tensile stresses in the cement around the tip of the keel went up to 11.5 MPa. So, the cement stresses, or the maximum cement stresses in case of metal backed design was higher than that of the total polyethylene design.

(Refer Slide Time: 52:29)



If we actually look into sectional plots in order to compare the stress distribution within the cancellous bone, we can also gain an insight into the load transfer by looking at these stretched sectional plots of the equivalent stress distribution. Now, you can see here total polyethylene design equivalent stress distribution in section through the glenoid has been plotted, the same section has been plotted or used to plot the stress distribution within the metal-backed polyethylene and the same section has been used for the uncemented case with a thicker, far more thicker metal backing.

The given stress distribution actually varied between say point 1 to 25 MPa maximum. So, in case of total polyethylene design, we can see the load is transferred from the processes through the cancellous bone it is distributed within the bone structure. In comparison, if we look at the stress distribution in the metal backed design, we see that due to the presence of the rigid metal backing, we see some amount of stress shielding being generated in case of the metal backed design.

So, the stresses are generated more within the implant, leaving the underlying bone to a low level of stress as compared to the total polyethylene design. In case of the unsegmented glenoid component, high stresses were generated within the implant. This comparison in equivalent stress distributions as presented here in the slide as sectional plots actually help to figure out the differences in the amount of stress shielding due to changes in glenoid component designs.

(Refer Slide Time: 55:18)

A Summary of Findings: Glenoid Prosthesis

- The cancellous bone, underlying the uncemented prosthesis is subject to lower stresses as compared to the cemented designs, which might result in stress shielding and adverse bone remodelling.
- For total PE and MB designs, the cement-bone interface adjacent to the tip of the keel appears very likely to fail (FL= 1.86, 2.16), as compared to the superior edge of the prosthesis (FL= 0.19, 0.68).
- The implant-bone interface, for the uncemented design appears less probable to fail (FL= 0.84) as compared to the cemented prostheses, since higher interface bond strength is offered.

NPTEL Online Certification Courses
IIT Kharagpur

So, we come to the summary of findings for glenoid prostheses. The cancellous bone underlying the uncemented processes is subject to lower stresses as compared to the cemented design which might result in stress shielding and adverse bone remodelling. For total polyethylene and metal-backed designs, the cement bone interface adjacent to the tip of the keel appears very likely to fail with FL values of about 1.86 and 2.16 as compared to the superior age of the prostheses, where we calculated FL values to be 0.19 and 0.68.

The implant-bone interface for the uncemented design appears less probable to fail, very interesting, FL equal to 0.84 as compared to the cemented prostheses. Since higher interface bond strength is offered in the case of uncemented design.

(Refer Slide Time: 56:37)

REFERENCES

- 1) Ghosh R., Pal B., Ghosh D. and Gupta S. (2013). Finite element analysis of a hemi-pelvis: the effect of inclusion of cartilage layer on acetabular stresses and strain. *Computer Methods in Biomechanics and Biomedical Engineering*, 18 (7), 697-710.
- 2) Gupta S. and Van der Helm F.C.T. (2004). Load transfer across the scapula during humeral abduction. *Journal of Biomechanics*, 37 (7), 1001 – 1009.
- 3) Gupta S., Van der Helm F.C.T., Van Keulen F. (2004a). Stress analysis of cemented glenoid prostheses in Total Shoulder Arthroplasty. *Journal of Biomechanics*, 37(11), 1777 – 1786.
- 4) Gupta S., Van der Helm F.C.T., Van Keulen F. (2004b). The possibilities of uncemented glenoid prosthesis – a finite element study. *Clinical Biomechanics*, 19(3), 292-302.

REFERENCES

- 5) Mathai, B. and Gupta, S. (2020). The influence of loading configurations on numerical evaluation of failure mechanisms in an uncemented femoral prosthesis. *Int J Numerical Methods Biomedical Engineering*, 36(8), e3353.
- 6) Pal B., Gupta S., New A.M.R. (2010). Influence of the change in stem length on the load transfer and bone remodelling for a cemented resurfaced femur, *Journal of Biomechanics*, 43 (15), 2908 – 2914.
- 7) Pal B., Gupta S., New A.M. (2009). A numerical study of failure mechanisms in the cemented resurfaced femur – effects of interface characteristics and bone remodelling. *Journal of Engineering in Medicine, Proc Instn Mech Engrs: Part H*, 223(4), 470 – 484.
- 8) Van der Helm F. C. (1994). A finite element musculoskeletal model of the shoulder mechanism. *Journal of Biomechanics*, 27(5), 551–569. [https://doi.org/10.1016/0021-9290\(94\)90065-5](https://doi.org/10.1016/0021-9290(94)90065-5)

The list of references are indicated in two slides, based on which the lecture was prepared.

Thank you for listening.